catalysts

MDPI

Article

Hydroxyl-Decorated Diiron Complex as a [FeFe]-Hydrogenase Active Site Model Complex: Light-Driven Photocatalytic Activity and Heterogenization on Ethylene-Bridged Periodic Mesoporous Organosilica

Juan Amaro-Gahete [1], Dolores Esquivel [1], Mariia V. Pavliuk [2], César Jiménez-Sanchidrián [1], Haining Tian [2], Sascha Ott [2,*] and Francisco J. Romero-Salguero [1,*]

[1] Departamento de Química Orgánica, Edificio Marie Curie, Facultad de Ciencias, Campus Universitario de Rabanales, Instituto Universitario de Nanoquímica (IUNAN), Universidad de Córdoba, 14071 Córdoba, Spain; q22amgaj@uco.es (J.A.-G.); q12esmem@uco.es (D.E.); qo1jisac@uco.es (C.J.-S.)

[2] Ångström Laboratories, Department of Chemistry, Uppsala University, P.O. Box 523, 751 20 Uppsala, Sweden; mariia.pavliuk@kemi.uu.se (M.V.P.); haining.tian@kemi.uu.se (H.T.)

* Correspondence: sascha.ott@kemi.uu.se (S.O.); qo2rosaf@uco.es (F.J.R.-S.); Tel.: +34-957-218638 (F.J.R.-S.)

Abstract: A biomimetic model complex of the [FeFe]-hydrogenase active site (FeFeOH) with an ethylene bridge and a pendant hydroxyl group has been synthesized, characterized and evaluated as catalyst for the light-driven hydrogen production. The interaction of the hydroxyl group present in the complex with 3-isocyanopropyltriethoxysilane provided a carbamate triethoxysilane bearing a diiron dithiolate complex (NCOFeFe), thus becoming a potentially promising candidate for anchoring on heterogeneous supports. As a proof of concept, the NCOFeFe precursor was anchored by a grafting procedure into a periodic mesoporous organosilica with ethane bridges (EthanePMO@NCOFeFe). Both molecular and heterogenized complexes were tested as catalysts for light-driven hydrogen generation in aqueous solutions. The photocatalytic conditions were optimized for the homogenous complex by varying the reaction time, pH, amount of the catalyst or photosensitizer, photon flux, and the type of light source (light-emitting diode (LED) and Xe lamp). It was shown that the molecular FeFeOH diiron complex achieved a decent turnover number (TON) of 70 after 6 h, while NCOFeFe and EthanePMO@NCOFeFe had slightly lower activities showing TONs of 37 and 5 at 6 h, respectively.

Keywords: [FeFe]-hydrogenase; periodic mesoporous organosilica; biomimetic chemistry; artificial photosynthesis; light-driven hydrogen evolution

Citation: Amaro-Gahete, J.; Esquivel, D.; Pavliuk, M.V.; Jiménez-Sanchidrián, C.; Tian, H.; Ott, S.; Romero-Salguero, F.J. Hydroxyl-Decorated Diiron Complex as a [FeFe]-Hydrogenase Active Site Model Complex: Light-Driven Photocatalytic Activity and Heterogenization on Ethylene-Bridged Periodic Mesoporous Organosilica. *Catalysts* **2022**, *12*, 254. https://doi.org/10.3390/catal12030254

Academic Editor: Omer Yehezkeli

Received: 21 December 2021
Accepted: 22 February 2022
Published: 23 February 2022

1. Introduction

The current energy crisis produced by the imminent depletion of non-renewable energy sources has prompted the scientific community to carry out numerous investigations with the aim of finding inexhaustible and environmentally friendly alternative energy forms [1–3]. In this area, solar energy applied to the chemical decomposition of an abundant substrate such as water is constantly on the rise as a key strategy for obtaining hydrogen [4–8].

A large part of the energy-sustainable systems of the future is based on hydrogen as a renewable energy carrier due to its high energy density and its combustion free of polluting gases [9,10]. The naturally occurring [FeFe]-hydrogenase enzymes in certain algae and bacteria catalyze the reduction of protons to hydrogen with a very high efficiency [11–13]. Due to the low availability of natural hydrogenases, a large number of investigations have been reported in the search for biomimetic catalysts reproducing the biological activity carried out by these enzymes, with the aim of designing an artificial photocatalytic system capable of providing light-driven hydrogen production [14,15].

Bimolecular reactions where electron transfer occurs between biomimetic [2Fe2S]-hydrogenase-based catalysts and suitable photosensitizers in the presence of an electron donor have been extensively investigated [16,17]. For these photocatalytic systems, a wide variety of molecular [2Fe2S] catalysts have been designed through well-established strategies and evaluated in photocatalytic reactions for hydrogen generation. Very different catalytic performances were reported to be dependent on the biomimetic diiron model and experimental conditions set for the photocatalytic system [18–27]. Regarding [2Fe2S] active sites, the structural modifications through ligand replacement in the first coordination sphere or incorporation of functionalities via the dithiolate-bridged group in the second coordination sphere have provided some interesting characteristics to the diiron complex. Among them, it is worth mentioning that the modulation of redox properties, photostability, water solubility and the inclusion of a specific functional unit allow for the formation of supramolecular architectures or the subsequent immobilization into heterogeneous solids [28–30].

Accordingly, the scientific community has made enormous efforts to the preparation of functional biomimetic systems based on [FeFe]-hydrogenase by modifying the first, second, or even outer coordination sphere [28,31–34], thus being capable of acting as artificial proton reduction catalysts in hydrogen evolution reactions. In fact, we have recently reported a comprehensive review of [FeFe]-hydrogenase-inspired catalysts applied in photocatalytic hydrogen production, including molecular [2Fe2S] catalysts, photosensitizer–[FeFe]-hydrogenase dyads, electron donor–photosensitizer–[FeFe]-hydrogenase triads, supramolecular entities, hybrid semiconductor assemblies, heterogeneous supports and photocathodes based on [2Fe2S] for photoelectrochemical (PEC) devices. Indeed, there exists growing interest in this research topic in order to design an efficient and effective catalytic architecture that exhibits high performance in the photochemical proton reduction to molecular hydrogen [35].

In the current work, the second coordination sphere of a hydroxyl-decorated diiron complex (FeFeOH; Figure 1a) [36] has been modified by the reaction with 3-isocyanopropyltriethoxysilane, providing a carbamate triethoxysilane bearing a diiron dithiolate biomimetic model (Figure 1b). The monosilane precursor obtained (NCOFeFe) was postulated as a promising candidate to be anchored on a silica-based support via outer coordination sphere interactions. Therefore, the precursor NCOFeFe was anchored in a periodic mesoporous organosilica (PMO) with ethylene-bridged organic groups using a grafting procedure (EthanePMO@NCOFeFe). Once characterized in detail, all the samples were tested as catalysts for light-driven hydrogen generation. The photocatalytic process was optimized in a homogeneous phase using the FeFeOH complex as the catalyst, $[Ru(bpy)_3]^{2+}$ as the photosensitizer, and ascorbic acid as the sacrificial electron donor under the irradiation with a light-emitting diode (LED) light and operating in an organic water/acetonitrile mixture (11.8 vol%). Different parameters influencing the reaction were evaluated in order to establish the optimal experimental conditions: pH, photon flux, and the concentration of catalyst or photosensitizer. The light source was changed to a Xenon lamp with a higher irradiation power to analyze the increase in the light intensity illuminated on the active area of the sample in the hydrogen production. The maximum TON of 70 was reached after 6 h for the molecular FeFeOH complex, almost 15 times higher compared to that obtained using the LED lamp. Conversely, the NCOFeFe precursor provided approximately half of the photocatalytic activity compared to FeFeOH, resulting in a TON of 37 for 6 h, while the heterogeneous catalyst EthanePMO@NCOFeFe yielded a lower TON of 5 after 6 h working in a pure aqueous medium. Such TONs are comparable to those reported for related systems in heterogeneous supports in the literature [35].

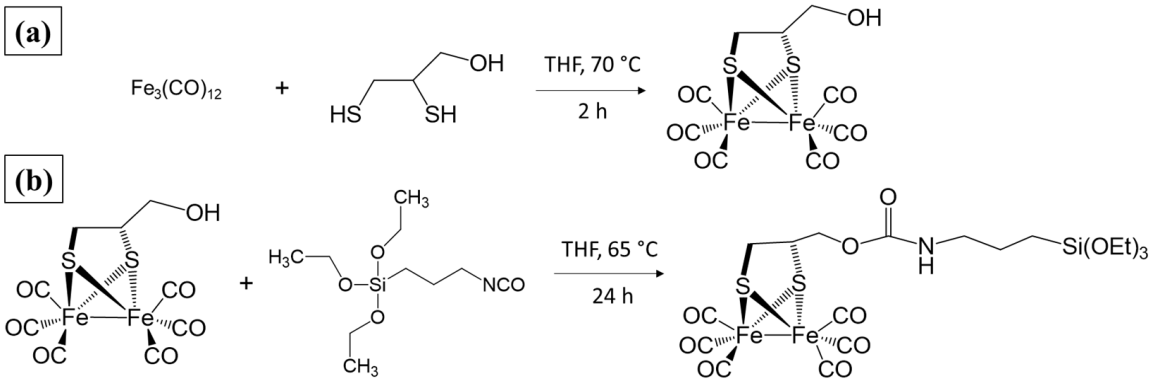

Figure 1. Schematic representation for the synthesis of the complex FeFeOH (**a**) and the monosilane precursor NCOFeFe (**b**).

2. Results and Discussion

2.1. Synthesis and Characterization of Diiron Catalysts

Figure 1 shows the reaction scheme for the synthesis of the FeFeOH hydroxyl–diiron complex and the monosilane precursor NCOFeFe. Firstly, FeFeOH was synthesized by the reaction of $Fe_3(CO)_{12}$ with 2,3-dimercapto-1-propanol in tetrahydrofuran (THF) under a nitrogen atmosphere at 70 °C for 2 h. The pendant hydroxyl group incorporated in the dithiolate bridge was of great interest due to the possibility of carrying out a subsequent functionalization. Accordingly, the monosilane precursor NCOFeFe was prepared via the reaction of FeFeOH and 3-isocyanatepropyltriethoxysilane in THF under a nitrogen atmosphere at 65 °C. The formation of the NCOFeFe precursor was monitored by FTIR-attenuated total reflection (ATR) taking aliquots of 100 µL at different times during 24 h (Figure S1). The progress of the reaction was corroborated by observing the disappearance of the isocyanate band over 2300 cm^{-1} and the concurrent growth of a new band corresponding to the C=O vibration from urethane at ca. 1715–1730 cm^{-1}. The molecular structures of the FeFeOH diiron complex and the NCOFeFe precursor were confirmed by proton and carbon nuclear magnetic resonance (^{1}H-NMR, ^{13}C-NMR, and ^{13}C DEPT-NMR; Figures S2–S5).

The FTIR-ATR spectra of 3-isocyanatopropyltriethoxysilane, FeFeOH, and NCOFeFe are shown in Figure 2a. The FeFeOH spectrum showed the characteristic bands corresponding to the C–O stretching vibrations located at 1994, 2034, and 2076 cm^{-1} for the diiron–hexacarbonyl complexes, while modes with the predominant Fe–CO characteristic appeared above 500 cm^{-1} [36,37]. The formation of the carbamate bond was confirmed by the presence of the vibration relative to the carbonyl groups C=O from the urethane group at 1715-1730 cm^{-1}, and the disappearance of the intense band peaked at ca. 2260 cm^{-1} related to the isocyanate group (N=C=O), which was observed in the starting reagent 3-isocyanatepropyltriethoxysilane [38]. The C–O stretching vibrations were located at similar wavelengths (1994, 2034, and 2076 cm^{-1}) as for FeFeOH, and the Fe–CO vibration modes were also present slightly above 500 cm^{-1}. The presence of the N–H stretching vibration in the range of 3200–3400 cm^{-1} and the N–H bending located above 1510 cm^{-1} were also observed. Furthermore, the C–H stretching of the hydrocarbon chain, the CO group from the carbamate, and the Si–O stretching of the triethoxysilane groups located at 2850–3000, 1235, and 1080 cm^{-1}, respectively, were present in the NCOFeFe precursor, similar to 3-isocyanatepropyltriethoxysilane, confirming the efficient functionalization process on the FeFeOH diiron complex.

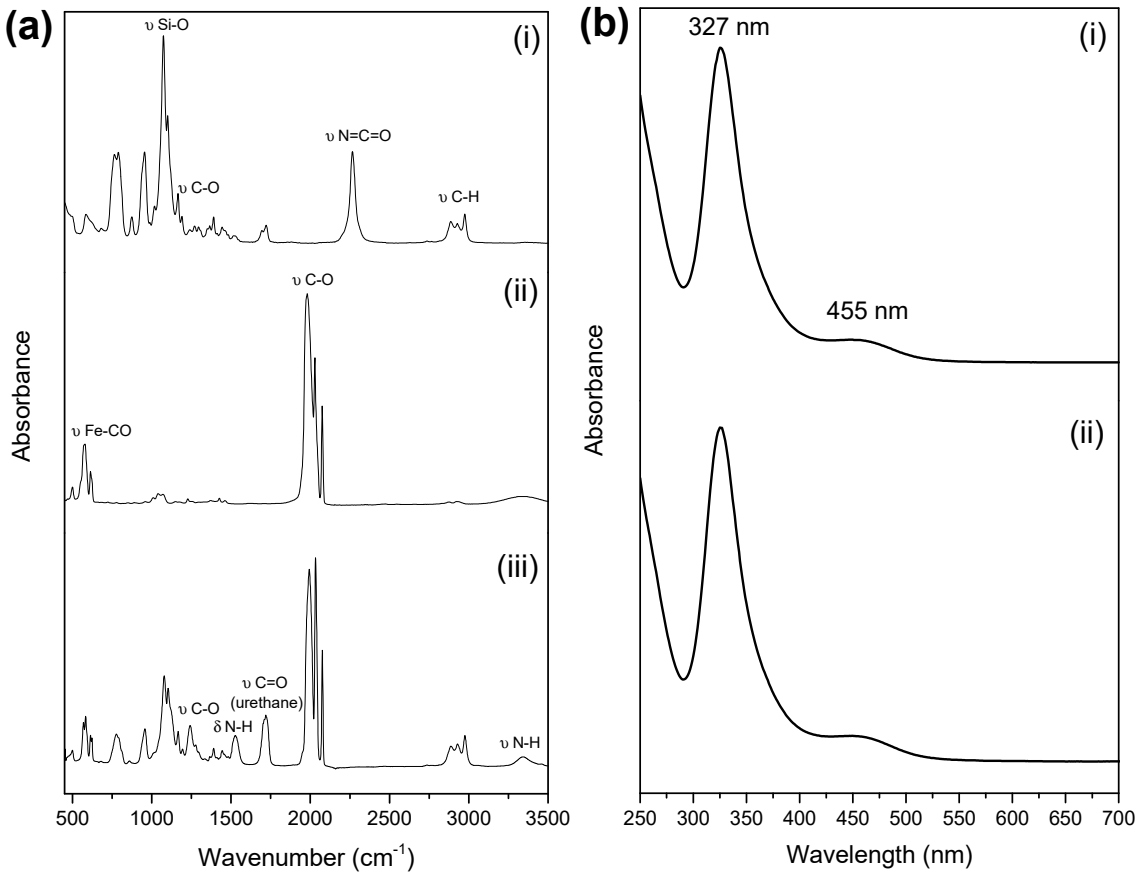

Figure 2. (**a**) FTIR-attenuated total reflection (ATR) spectra of 3-isocyanatopropyltriethoxysilane (**i**), FeFeOH (**ii**), and NCOFeFe (**iii**). (**b**) UV-VIS spectra of FeFeOH (**i**) and NCOFeFe (**ii**).

The UV–VIS absorption spectrum of FeFeOH and NCOFeFe were recorded in CH_2Cl_2 at room temperature. As shown in Figure 2b, both compounds exhibited two identical bands centered at 327 cm^{-1} (UV region) and 455 cm^{-1} (visible region) assigned to π–π* electronic transitions and metal-to-ligand charge-transfer (MLCT) transitions, respectively [39–43]. Therefore, the functionalization of the FeFeOH complex did not generate significant alterations in the electron densities at the diiron core, which corroborated the results drawn from the FTIR-ATR measurements.

Periodic mesoporous organosilicas (PMOs) are organic–inorganic hybrid materials prepared by the condensation of a hydrolysable bis-silane of the type $(R'O)_3$-Si-R-Si-$(OR')_3$, where R is the organic functional linker located within the channel walls as bridges between silicon centers and R´ is a hydrolysable group (normally ethoxy or methoxy), in the presence of a surfactant that acts as a structure-directing agent. Ethylene-bridged periodic mesoporous organosilicas (EthanePMO) are the most readily available materials of the PMO family. They show interesting features such as high hydrophobicity and high mechanical and hydrothermal stability in aqueous media [44]. Therefore, this material was chosen as the support for the diiron complexes. Thus, the NCOFeFe precursor was anchored onto EthanePMO by a grafting method at room temperature for five days using $CHCl_3$ as the solvent (Figure 3). The structural analysis of EthanePMO@NCOFeFe taking the starting EthanePMO as a reference was examined by XRD, FTIR-ATR spectroscopy, UV-VIS diffuse reflectance spectroscopy, TEM, and nitrogen adsorption isotherm analyses.

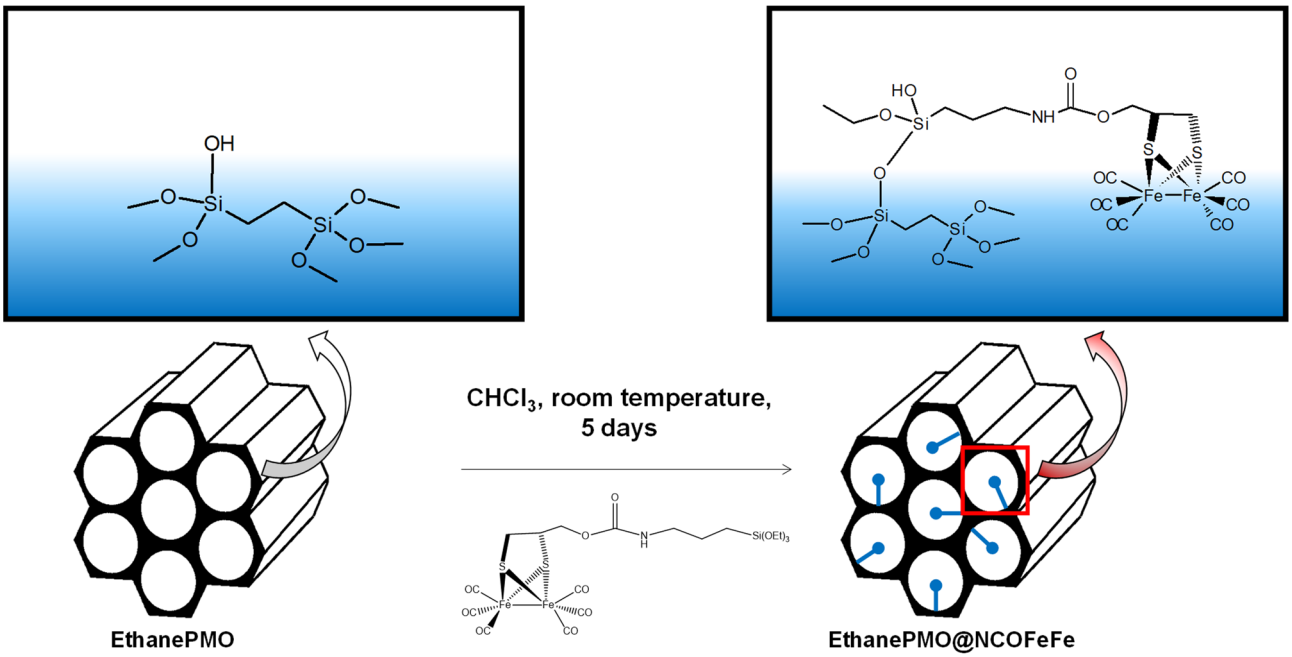

Figure 3. Scheme of the grafting procedure on the ethylene-bridged periodic mesoporous organosilicas (EthanePMO) material with the NCOFeFe precursor.

The XRD patterns of EthanePMO and EthanePMO@NCOFeFe are shown in Figure 4a. Both diffractograms exhibited a strong reflection at a low angle ($2\theta \approx 1^{\circ}$) related to the (100) diffraction peak from a two-dimensional (2D) hexagonal structure and two weak well-defined diffraction peaks corresponding to (110) and (200) planes, typical of a *p6mm* mesostructure [45]. The incorporation of the NCOFeFe monosilane precursor into the EthanePMO support was confirmed by FTIR-ATR and UV-VIS spectroscopic techniques. The FTIR-ATR spectra of EthanePMO@NCOFeFe represented in Figure 4b contained three prominent C–O stretching vibration bands at 1998, 2046, and 2080 cm^{-1}, while no such peaks were observed for EthanePMO in the range of 1600–2400 cm^{-1}. The solid-state UV−VIS spectra of EthanePMO@NCOFeFe (Figure 4c) also showed two characteristic absorption bands at 329 and 457 cm^{-1}, which were in accordance with the UV-VIS spectral features of the NCOFeFe and FeFeOH diiron complexes. No absorption bands were appreciated in the UV–VIS diffuse reflectance spectrum of EthanePMO. The results clearly confirmed that the NCOFeFe precursor was successfully attached to the surface of EthanePMO with a grafting procedure. The loading of iron in the EthanePMO@NCOFeFe material determined by inductively coupled plasma mass spectrometry (ICP-MS) was 0.235 mmol Fe/g PMO.

The nitrogen adsorption/desorption isotherms and pore size distributions of EthanePMO and EthanePMO@NCOFeFe are shown in Figure 5. Both materials exhibited type IV isotherms with H1-type hysteresis loops with a sharp step at P/P_0 around 0.6–0.8, typically obtained for ordered mesoporous materials with uniform pores [46,47]. These results corroborated that the ordered mesoporous structure was essentially preserved after anchoring the NCOFeFe precursor. The pore size distribution represented for both materials mainly indicated the presence of pores in the meso range and a reduced fraction of micropores.

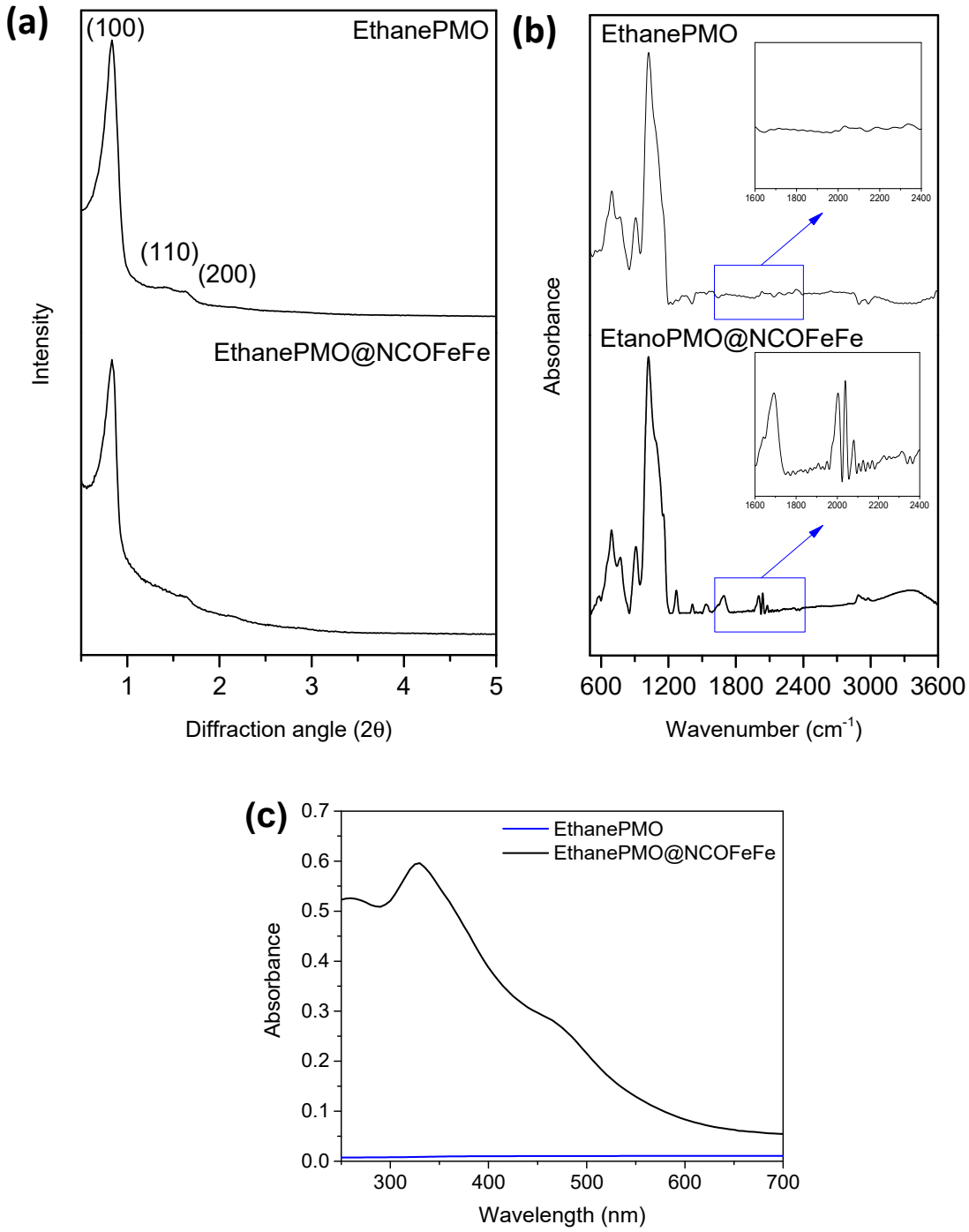

Figure 4. XRD patterns (**a**), FTIR-ATR spectra (**b**), and UV–VIS diffuse reflectance spectra (**c**) of EthanePMO and EthanePMO@NCOFeFe.

The Brunauer–Emmett–Teller (BET) surface areas (S_{BET}), density functional theory (DFT) pore diameters (D_p) and volumes (V_p), and t-plot micropore analysis data, determined from isotherms, are listed in Table 1. The EthanePMO@NCOFeFe material exhibited a decreased BET surface area (481 m^2/g), pore diameter (4.9 nm), and pore volume (0.55 cm^3/g) compared to the pristine EthanePMO, demonstrating the efficient attachment of the NCOFeFe monosilane precursor during the grafting process. Additionally, the area and volume of micropores were also reduced, suggesting the blockage of micropores upon the incorporation of the NCOFeFe compound into the walls.

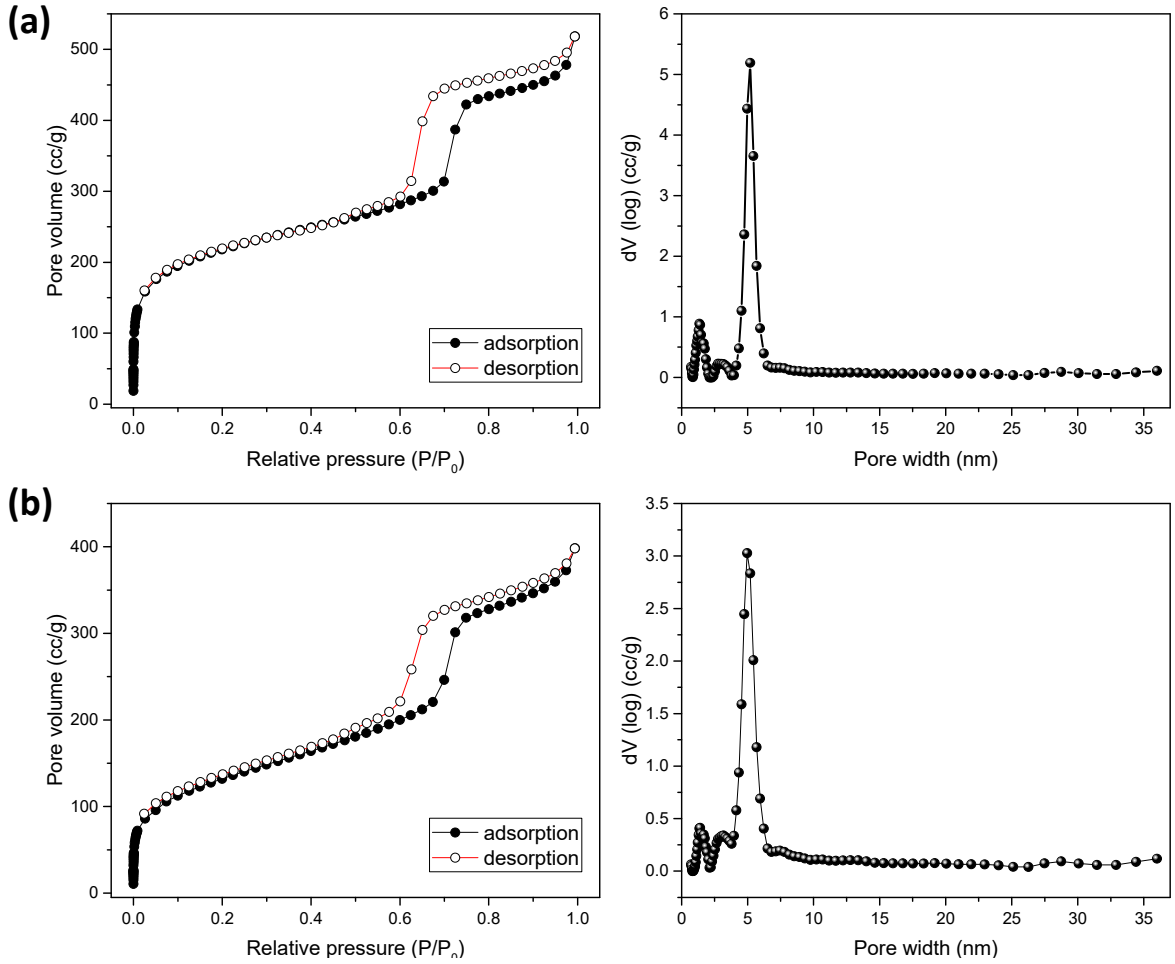

Figure 5. Nitrogen adsorption–desorption isotherms (left) and pore size distributions calculated by the density functional theory (DFT) method (right) of EthanePMO (**a**) and EthanePMO@NCOFeFe (**b**).

Table 1. Textural properties of EthanePMO and EthanePMO@NCOFeFe materials.

Sample	Brunauer–Emmett–Teller (BET) Surface Area (m^2/g)	D_p (nm) [a]	V_p (cm^3/g) [a]	External Surface Area (m^2/g) [b]	Micropore Area (m^2/g) [b]	Micropore Volume (cm^3/g) [b]
EthanePMO	789	5.2	0.71	363	426	0.18
EthanePMO@NCOFeFe	481	4.9	0.55	375	106	0.04

[a] analysis by the DFT method. [b] t-plot method micropore analysis.

To further characterize the PMO materials, the morphology was analyzed by TEM (Figure 6). The TEM images clearly confirmed the preservation of the characteristic mesoporous structure after the grafting procedure, in agreement with the analysis carried out by XRD and N_2 adsorption–desorption measurements. Both the starting EthanePMO and the EthanePMO@NCOFeFe exhibited 2D parallel-aligned cylindrical mesopore channels with a honeycomb-like arrangement, uniform sizes, and hexagonal shapes [48–50]. In addition, no particles deposited on the walls or inside the pores of the material were observed, confirming the absence of aggregates from NCOFeFe species on PMO.

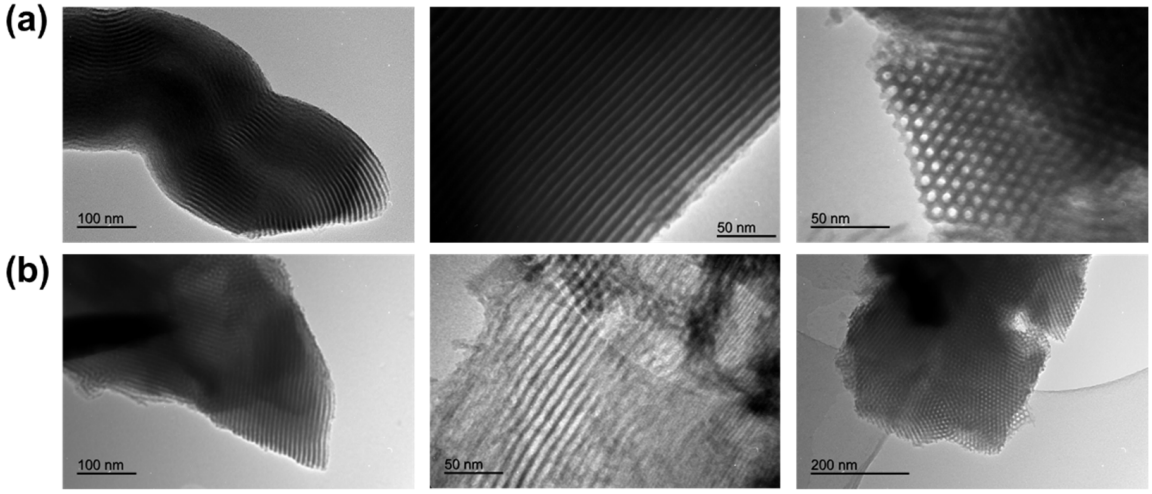

Figure 6. TEM images of EthanePMO (**a**) and EthanePMO@NCOFeFe (**b**).

2.2. Light-Driven Hydrogen Production

Light-driven hydrogen production was examined using FeFeOH as the catalyst, $[Ru(bpy)_3]^{2+}$ as the photosensitizer, and ascorbic acid as the sacrificial electron donor under white LED irradiation (50 mW/cm^2, λ = 475–750 nm). Due to the poor solubility of the diiron complex in pure water, a slight proportion of acetonitrile (11.8 vol%) was added to the total volume of the reaction mixture in order to ensure the complete dissolution of the catalyst.

As depicted in Figure 7, the proposed scheme for photocatalytic proton reduction by the FeFeOH catalyst commences with the reductive quenching of excited $*[Ru(bpy)_3]^{2+}$ by the ascorbate electron donor according to the mechanism reported for other $[Ru(bpy)_3]^{2+}$/ascorbate systems [51,52]. The photogenerated $[Ru(bpy)_3]^{+}$ successively reduces the catalyst by the transfer of one electron, recovering the original state of the photosensitizer. Once this process is repeated a second time, two electrons are accumulated at the FeFeOH diiron catalyst, and two protons will be reduced to one H_2 molecule. This process is thermodynamically feasible based on the cathodic peak potential of FeFeOH (−1.18 V vs. Ag/AgCl) [53] which is sufficiently mild to be accessed from the photo-produced $[Ru(bpy)_3]^{+}$ reductant. In fact, this light-driven electron transfer process bears resemblance to other related works in which a sufficient driving force for electron transfer from photo-reduced $[Ru(bpy)_3]^{+}$ to diiron catalysts following the photocatalytic mechanism mentioned above is established [19,24].

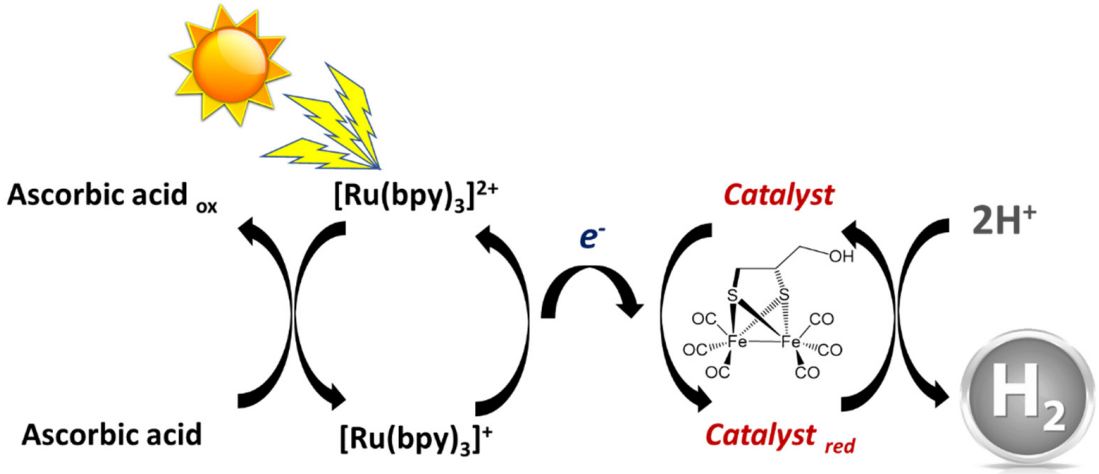

Figure 7. Schematic representation of light-driven hydrogen production by the FeFeOH catalyst.

In order to optimize the experimental conditions of the photocatalytic system, light-induced hydrogen evolution was conducted by modifying the pH, the percentage of photon flux, and the concentrations of the diiron catalyst and the photosensitizer. The pH value of the catalytic system was adjusted with a 1 M acetate buffer at pH 4.5, 5.0, and 5.5. Under standard conditions (0.084 mM of FeFeOH, 0.5 mM of $Ru(bpy)_3^{2+}$, and 100 mM of ascorbic acid), the highest catalytic activity was accomplished at pH 5.0, resulting in a TON of 4.8 after 2 h (Figure 8). While similar results were obtained at pH 5.5, the poorer photocatalytic performance at lower pH values (pH = 4.5) is most likely due to the increasing amount of ascorbate being in its protonated state (pK_{a1} = 4.17), in which it is known to be a significantly weaker donor to $*[Ru(bpy)_3]^{2+}$ than in its deprotonated state.

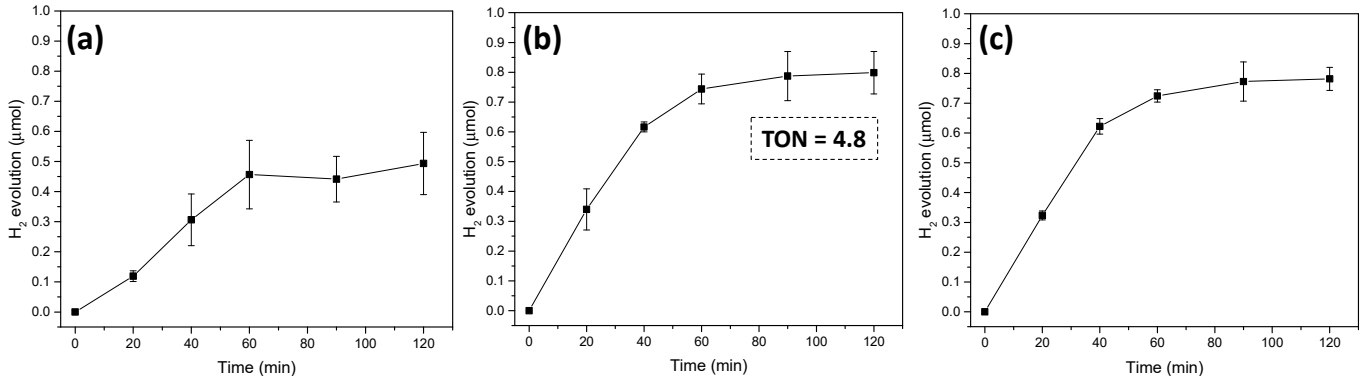

Figure 8. Photocatalytic hydrogen production as a function of the pH: (**a**) 4.5; (**b**) 5.0; and (**c**) 5.5.

The photon flux was a parameter that was tuned to determine the limitation of the system related to the light intensity projected on the surface of the photocatalytic system. These experiments were carried out by placing two neutral density filters (60% transmittance and 30% transmittance) in front of the LED lamp (Figure 9). Minor deviations of the hydrogen evolution were observed with the 60% transmittance filter compared to the reaction without any filter (within the error). In contrast, a further decrease of the light intensity up to 30% transmittance produced a reduction of hydrogen gas evolution over 40%. Therefore, when the photon flux from the LED lamp was less than 60%, the hydrogen productivity generated by the photocatalytic system was decreased. These findings corroborated that the photocatalytic activity of FeFeOH under these conditions was limited by photon flux.

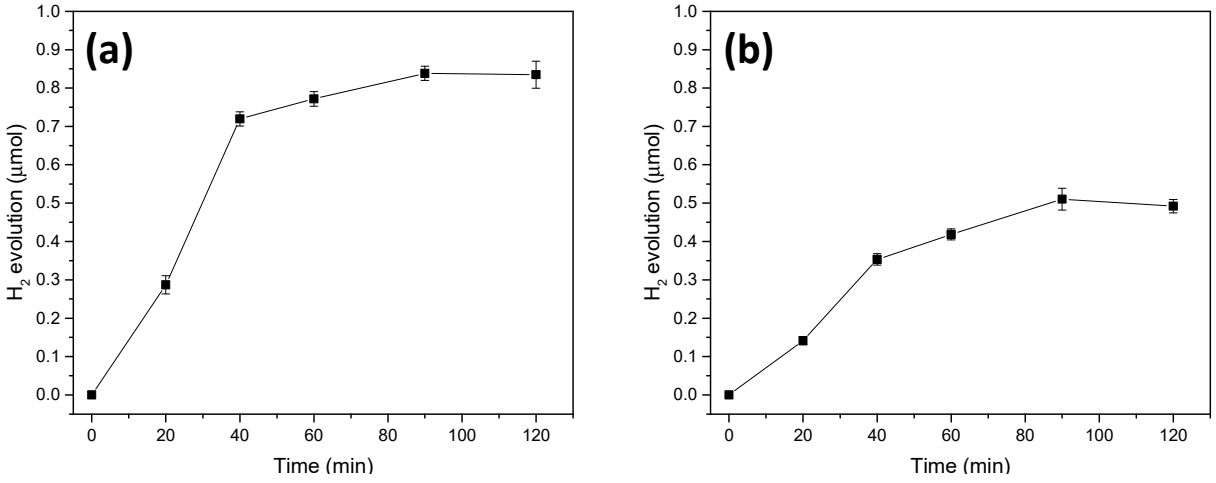

Figure 9. Hydrogen evolution data for the FeFeOH photocatalytic system at pH 5.0 with neutral density filters that transmitted 60% (0.2 mm thickness) (**a**) and 30% (0.5 mm thickness) (**b**) of the initial light.

The light-driven hydrogen evolution catalyzed by FeFeOH at different concentrations while maintaining the standard conditions of the photosensitizer and the electron donor at pH = 5.0 for 2 h is illustrated in Figure 10a. The results indicated that the overall hydrogen production increased linearly with the catalyst concentration from 0.0084 to 0.168 mM. This behavior favors photocatalytic performance at high catalyst concentrations for large-scale hydrogen generation [54]. Accordingly, Figure 10b shows the initial rate of H_2 formation (µmol of H_2 min^{-1}) versus the catalyst concentration (mM). The linear dependence observed between both parameters indicated a pseudo first-order reaction [55]. The influence of $[Ru(bpy)_3]^{2+}$ photosensitizer concentration on the photoinduced hydrogen production is represented in Figure 10c. Under standard conditions, hydrogen evolution decreased by 40% at a lower photosensitizer concentration. Interestingly, an increased productivity was not observed, when the photosensitizer concentration was doubled, thus suggesting that the performance of the photocatalytic reaction was not restricted by the $[Ru(bpy)_3]^{2+}$ concentration. Control experiments in the absence of the FeFeOH catalyst and the photosensitizer generated minimal amounts of hydrogen, indicating that all components were essential for hydrogen production (Figure S4). The photocatalytic activity of the NCOFeFe monosilane precursor was also tested. As shown in Figure 10d, NCOFeFe provided a similar hydrogen evolution compared to the FeFeOH diiron complex under standard conditions at pH 5.0. Therefore, the functionalization of the FeFeOH did not affect the photocatalytic performance under the standard experimental conditions established for the photocatalytic reaction.

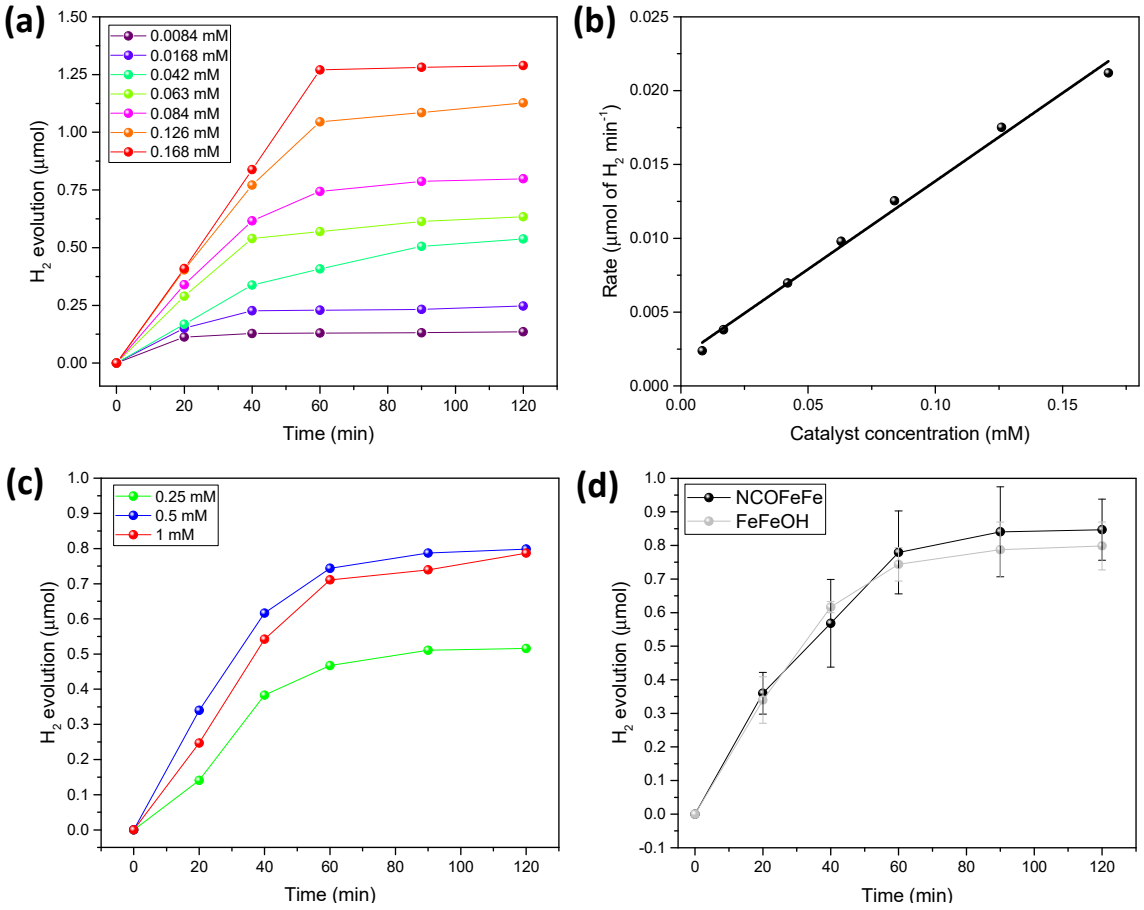

Figure 10. (**a**) Photocatalytic hydrogen production as a function of the FeFeOH catalyst concentration at pH = 5.0; (**b**) initial rate of H_2 formation versus the concentration of the FeFeOH catalyst obtained from the previous graph; (**c**) photocatalytic hydrogen production as a function of the $[Ru(bpy)_3]^{2+}$ photosensitizer concentration at pH = 5.0; and (**d**) comparison of the photocatalytic hydrogen productions between FeFeOH and NCOFeFe catalysts at pH = 5.0.

Once the experimental conditions of the photocatalytic reaction were optimized for homogeneous catalysis, the light source was replaced by a Xenon lamp with a higher irradiation intensity to evaluate the effect of this parameter on the photocatalytic performance. The Xe lamp provided a higher light intensity illuminated on the active area of the sample of 90 mW/cm^2 and an increased range of wavelength ($\lambda > 420$ nm) to cover most of the maximum absorption of the photosensitizer $[Ru(bpy)_3]^{2+}$ [56]. As can be seen in Figure 11, the FeFeOH complex reached the maximum TON of 70 after 6 h, which is amongst the highest reported catalytic performances of diiron catalysts under similar experimental conditions, using $[Ru(bpy)_3]^{2+}$ as the photosensitizer and ascorbate as the sacrificial electron donor (Table S1). A lower TON of 37 was obtained for NCOFeFe under the same standard conditions for 6 h, demonstrating a loss of photocatalytic activity of around 50% with respect to FeFeOH. We assigned this drop in activity either to a lower intrinsic activity of the NCOFeFe catalyst or non-productive reduction events at the NCOFeFe catalyst that may involve the reduction of the carbamate tether. The FeFeOH complex displayed an excellent solubility under reaction conditions, thus providing a good accessibility of diiron active sites for promoting an efficient electron transfer from the photo-reduced $[Ru(bpy)_3]^{+}$. The molecular aggregation phenomena of the NCOFeFe precursor might, however, occur during the photocatalytic reaction due to its hydrophobic chain, thus causing a restricted availability of diiron active sites capable of being reduced, thereby offering another potential explanation for the decreased hydrogen production performance. Obtaining an analogous TON for FeFeOH and NCOFeFe under the lighting system with an LED lamp could be explained by the lower irradiation intensity emitted on the photocatalytic system, which would cause a lower concentration of reduced $[Ru(bpy)_3]^{+}$ species. Therefore, in both cases, sufficient diiron active sites would be present to achieve the maximum hydrogen productivity under these conditions. Furthermore, the photodegradation of the FeFeOH and NCOFeFe catalysts was observed spectroscopically after 4 h. The maximum absorption bands of both catalysts decreased and shifted drastically (Figure S7), while the original carbonyl groups completely disappeared in the FTIR-ATR spectra (Figure S8). This would cause the deactivation of the catalysts, thus preventing further hydrogen production.

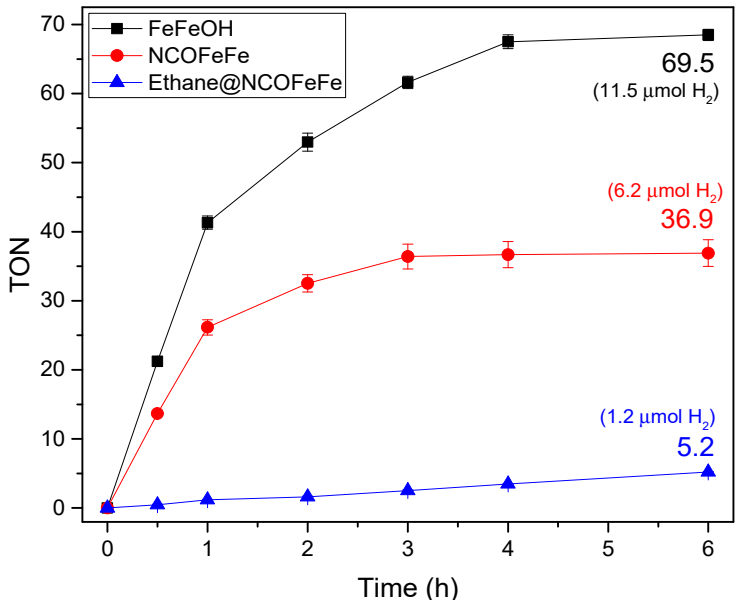

Figure 11. Photocatalytic hydrogen production under standard conditions (0.084 mM of the homogeneous catalyst, 0.5 mM of $Ru(bpy)_3^{2+}$, 100 mM of ascorbic acid, and 1 M of the acetate buffer at pH 5.0) in the homogeneous phase (ACN/H_2O with a 11.8 vol% organic phase) using FeFeOH and NCOFeFe. Similar conditions were stablished in the heterogeneous phase with the only difference being the solvent, i.e., milli-Q water solution, and using 2 mg of EthanePMO@NCOFeFe.

The heterogeneous catalyst EthanePMO@NCOFeFe was also evaluated under photocatalytic conditions using the Xenon lamp as a light source. The modulation of the outer coordination sphere on the NCOFeFe precursor by anchoring to EthanePMO material allowed working in pure aqueous solutions, which is one of the advantages of using heterogeneous supports incorporating biomimetic models of the [FeFe]-hydrogenase active site that are otherwise only soluble in organic solvents. Control experiments with pristine EthanePMO and without $[Ru(bpy)_3]^{2+}$ photosensitizer in the photocatalytic system were carried out, resulting in negligible hydrogen production. Unfortunately, the high photocatalytic activities shown by the FeFeOH complex and the NCOFeFe precursor were not achieved for the heterogeneous catalyst using analogous concentrations of diiron centers. Probably, the blocking of some diiron active sites could be the cause of the low photocatalytic performance, possibly as a consequence of the hydrophobic chain folding inside the channel walls of EthanePMO. Anyway, the activity of this heterogeneous catalyst, with a TON of 5.2, was comparable to other biomimetic models of the [FeFe]-hydrogenase active site anchored on heterogeneous supports reported in the literature for light-induced hydrogen generation [35]. Moreover, the immobilization of NCOFeFe on EthanePMO support promoted the stabilization of the diiron center, extending the photocatalytic activity for hydrogen evolution beyond 4 h (Figure S9).

3. Materials and Methods

3.1. Reagents and Materials

Triiron dodecacarbonyl (Fe_3CO_{12}, containing 1–10% methyl alcohol), 2,3-dimercapto-1-propanol (≥98%, iodometric), THF (anhydrous, ≥99.9%, inhibitor-free), ethyl acetate (ACS reagent, ≥99.5%), 3-isocyanatepropyltriethoxysilane (95%), poly(ethylene glycol)-block-poly(propylene glycol)-block-poly(ethylene glycol) (P123, average M_n: ~5800), potassium chloride (KCl, ACS reagent, 99.0–100.5%), hydrochloric acid (HCl, ACS reagent, 37%), 1,2-bis(triethoxysilyl)ethane (96%), L-ascorbic acid (ACS reagent, ≥99%), and tris(2,2′-bipyridyl)ruthenium(II) chloride hexahydrate ($Ru(bpy)_3{}^{2+}$, 99.5% trace metals basis) were purchased from Sigma-Aldrich (St. Louis, Missouri, United States). Hexane (alkanes mixture for analysis) was obtained from PanReac AppliChem (Barcelona, Spain). Petroleum ether (40–60 AGR), ethyl acetate (AGR, 99.5%), ethanol absolute (AGR, 96%), dichloromethane (CH_2Cl_2, amylene as stabilizer, AGR, 99.9%), and chloroform ($CHCl_3$, AGR, 98.5%) were purchased from Labbox Labware S.L. (Barcelona, Spain).

3.2. Synthesis of the Catalysts

The synthesis of the hydrogenase biomimetic model FeFeOH was carried out by adapting the procedure previously reported by Liu et al. [36]. In a three-neck round-bottom flask, a mixture of 2.42 g (4.8 mmol) Fe_3CO_{12}, 0.5 mL (4.8 mmol) 2,3-dimercapto-1-propanol, and 100 mL anhydrous THF was stirred at 70 °C for 4 h under a nitrogen atmosphere. Initially, the color of the solution was dark green, but it changed to dark red after the total reaction time was completed. After the mixture was cooled to room temperature, the solvent was evaporated with a rotary evaporator under reduced pressure. The crude product was purified by column chromatography using petroleum ether:ethyl acetate (4:1, *v/v*) as the eluent. The FeFeOH hydroxyl–diiron complex was crystallized from hexane/CH_2Cl_2 (2:1, *v/v*) at 4 °C as a red solid (1.7 g, yield: 88%). ^{1}H NMR (400 MHz, $CDCl_3$) δ 3.63 (m, 1H, C*H*H-OH), 3.53 (m, 1H, CH*H*-OH), 2.81 (m, 1H, CH), 2.66 (dd, *J* = 13.1, 7.7 Hz, 1H, C*H*H-CH), 1.91 (dd, J = 13.1, 5.6 Hz, 1H, CH*H*-CH), 1.85 (m, 1H, OH). ^{13}C NMR (76 MHz, $CDCl_3$) δ 65.36 (CH_2-OH), 56.06 (CH_2-*C*H), 38.71 (*C*H_2-CH). IR ($CHCl_3$, cm^{-1}): 1981, 2029, 2075. UV/VIS ($CHCl_3$, nm): 327, 455.

The monosilane hydrogenase precursor NCOFeFe was prepared by the reaction of FeFeOH and 3-isocyanatepropyltriethoxysilane. In a three-neck round-bottom flask was placed 0.8 g of FeFeOH (2.0 mmol) dissolved in 25 mL of anhydrous THF under a nitrogen atmosphere. The yellow solution was magnetically stirred at 65 °C under reflux. Subsequently, 1 mL of 3-isocyanatepropyltriethoxysilane was slowly added dropwise.

Then, the reaction was left to react under an inert atmosphere for 24 h and monitored by FTIR-ATR spectroscopy. Later, the solvent was evaporated with a rotary evaporator under reduced pressure, and the crude product was purified by column chromatography using hexane:ethyl acetate (4:1, *v/v*) as the eluent. The NCOFeFe monosilane precursor was obtained as a dark red viscous oil (0.9 g, yield: 67%). ^{1}H NMR (300 MHz, $CDCl_3$) δ 4.95 (s, 1H, NH), 3.94 (m, 2H, CH_2-O-), 3.75 (q, *J* = 7.0 Hz, 6H, O-CH_2-CH_3), 3.11 (q, *J* = 6.8 Hz, 2H, NH-CH_2-CH_2-CH_2-Si), 2.83 (m, 1H, CH), 2.58 (dd, *J* = 13.2, 7.7 Hz, 1H, C*H*H-CH), 1.87 (dd, *J* = 13.2, 5.7 Hz, 1H, CH*H*-CH), 1.55 (m, 2H, NH-CH_2-CH_2-CH_2-Si), 1.16 (t, *J* = 7.1 Hz, 9H, O-CH_2-CH_3), 0.55 (t, *J* = 8.1 Hz, 2H, NH-CH_2-CH_2-CH_2-Si). ^{13}C NMR (76 MHz, $CDCl_3$) δ 65.95 (*C*H_2-O), 59.91 (O-*C*H_2-CH_3), 52.86 (CH_2-*C*H), 43.71 (NH-*C*H_2-CH_2-CH_2-Si), 38.64 (*C*H_2-CH), 23.38 (NH-CH_2-*C*H_2-CH_2-Si), 19.23 (O-CH_2-*C*H_3), 7.85 (NH-CH_2-*C*H_2-CH_2-Si). IR ($CHCl_3$; cm^{-1}): 1994, 2034, 2076. UV/VIS ($CHCl_3$; nm): 327, 455.

Periodic mesoporous organosilica EthanePMO was synthesized following the procedure reported by Yang et al. [57]. Typically, 3.3 g of P123 and 20.94 g of KCl were stirred in 99 g of HCl (2 M) and 22.5 g of H_2O at 45 °C for 24 h. After that, 1,2-bis(triethoxysilyl)ethane (7.55 mL, 21.3 mmol) was added dropwise to the formed solution. The reaction mixture was left under stirring at 45 °C for 24 h and then aged at 100 °C under static conditions for 24 h. The white suspension was filtered and washed with distilled water and ethanol. The solid was dried under vacuum at 80 °C overnight. Surfactant extraction was performed by refluxing 1 g of the as-synthesized material in a solution of 1 mL HCl in 50 mL ethanol for 24 h at 80 °C. After repeating this process twice, 3.38 g of the white solid product EthanePMO were recovered by filtration, washed with ethanol and dried under vacuum at 120 °C. The grafting procedure of the NCOFeFe precursor on the EthanePMO matrix was similar to that described by Yang et al. [58]. Then, 6.98 g of NCOFeFe (10.8 mmol) were added dropwise into 1.28 g of EthanePMO previously dispersed in 100 mL of $CHCl_3$. The suspension was kept under stirring for 5 days. Afterwards, the solid was filtered, washed repeatedly with $CHCl_3$ and dried under vacuum at 60 °C. The material was referred to as EthanePMO@NCOFeFe.

3.3. Characterization of the Catalysts

The ^{1}H-NMR spectra were recorded at 300 MHz on a Bruker Avance III (AVIII, Bruker Corporation, Billerica, Massachusetts, United States) at room temperature. Chemical shifts were measured relative to a tetramethylsilane standard. The UV–VIS spectroscopy for the FeFeOH complex and the NCOFeFe precursor were performed in the liquid phase with a double-beam UV/VIS 4260/50 (ZUZI, Auxilab, Beriáin, Navarra) instrument in a wavelength range of 250–700 nm. The UV/VIS diffuse reflectance spectroscopy for solid samples was measured with a Perkin Elmer Lambda 650S UV/VIS spectrometer (PerkinElmer, Inc., Waltham, MA, USA) in a wavelength range of 250–700 nm. FTIR spectra were obtained on a PerkinElmer FTIR spectrometer (PerkinElmer, Inc., Waltham, MA, USA), equipped with a high-performance Pike GladiATR monolithic diamond crystal accessory (PIKE Technologies, Fitchburg, MA, USA) of the ATR mode. The XRD patterns of powdered solid samples were collected with a Bruker D8 Discover X-ray diffractometer using monochromatic Cu Kα radiation (λ = 1.5406 Å). The patterns were recorded within the 0.5–5° (2θ) range, using a step size of 0.040° and 1.05 s per step. Specific surface areas, pore sizes and pore volumes were examined from the N_2 adsorption–desorption isotherms with an Autosorb iQ/ASiQwin (Quantachrome Instruments, Moscow, Russia). The samples were previously outgassed under vacuum at 120 °C overnight and then measured at the liquid nitrogen temperature (77 K). Surface areas were calculated using the BET method. Pore size distributions and pore volumes were obtained from the DFT method. Micropore analysis was performed by the t-plot method. TEM images were obtained on a Jeol JEM-1400 transmission electron microscope (JEOL Ltd., Akishima, Tokyo, Japan) operated at an accelerating voltage of 120 kV. Iron loading was determined by ICP-MS analysis in an ICP Mass Spectrometer model NexIONTM 350X (PerkinElmer Inc., Waltham, MA, USA).

3.4. Photocatalytic Experiments

The optimization of photocatalytic hydrogen evolution was performed in 9 mL gastight vials containing 0.084 mM of the homogeneous catalyst, 0.5 mM of $Ru(bpy)_3^{2+}$, 100 mM of ascorbic acid, and 1 M of an acetate buffer at pH = 5.0 in a total volume of 2 mL using the solvent ACN/H_2O with a 11.8 vol% organic phase. Firstly, the solution was purged with argon (Ar) for 20 min in order to completely remove oxygen. An LED PAR38 lamp (17W, 5000K, Zenaro Lighting GmbH, Karlsruhe, Baden-Württemberg, Germany, λ = 475–750 nm) was used as the light source. The light intensity illuminated on the active area of the sample was 50 mW cm^{-2}, as measured by a pyranometer (CM11, Kipp&Zonen, B.V., Delftechpark, XH Delft, The Netherlands). The LED light source basically had a similar intensity to the standard 1 sun condition between 475 and 750 nm. After starting light irradiation, aliquots of 100 µL of the headspace were removed at different times using a gastight Hamilton syringe, and the amount of hydrogen evolved from the system was subsequently analyzed by gas chromatography (GC; PerkinElmer Clarus 500, PerkinElmer Inc., Waltham, MA, USA) using Ar as the carrier gas. The total reaction time was 2 h. The photocatalytic reactions were carried out three times, and the results were given as average values with standard deviations.

In addition, a Xenon lamp (300 W, λ > 420 nm; Ushio Inc., Tokyo, Japan) was used as the light source. In this case, the light intensity illuminated on the active area of the sample was 90 mW/cm^2. The reaction conditions in the homogeneous phase for the FeFeOH complex and the NCOFeFe precursor were the same as those mentioned above. In the case of the heterogeneous phase, 2 mg of EthanePMO@NCOFeFe were used, maintaining the same concentrations of $[Ru(bpy)_3]^{2+}$, the ascorbic acid, and the acetate buffer at pH = 5.0, but using a totally aqueous medium. Once the irradiation on the samples started, aliquots of 100 µL of the headspace were withdrawn at different times using a gastight Hamilton syringe and the amount of hydrogen evolved from the system was subsequently analyzed by GC (Shimadzu GC-2010 Plus, Shimadzu Corporation, Kyoto, Japan) using He as the carrier gas. The total reaction time was 6 h. The photocatalytic reactions were carried out four times, and the results were given as average values with standard deviations.

4. Conclusions

A biomimetic [FeFe]-hydrogenase active site model complex (FeFeOH) with an ethylene bridge and a pendant hydroxyl group has been successfully synthesized, characterized and investigated for the first time as a potential catalyst for light-driven hydrogen evolution. In addition, a novel precursor based on a carbamate triethoxysilane bearing a diiron dithiolate (NCOFeFe) was designed and prepared to be incorporated on a solid support. Thus, it was efficiently anchored onto EthanePMO via a grafting procedure, obtaining the EthanePMO@NCOFeFe material with an iron loading of 0.235 mmol Fe/g PMO.

The photocatalytic hydrogen production system was adequately optimized in the homogeneous phase using the FeFeOH complex as the catalyst, $[Ru(bpy)_3]^{2+}$ as the photosensitizer, and ascorbic acid as the electron donor in a water/acetonitrile mixture (11.8 vol%) under irradiation by an LED light with an intensity of 50 mW/cm^2. Different variables influencing the photocatalytic reaction were investigated: pH, photon flux, catalyst concentration, and photosensitizer concentration. Under these conditions, the NCOFeFe precursor showed similar hydrogen generation compared to the FeFeOH complex. The replacement of the lighting system by a Xenon lamp with a higher light intensity, i.e., 90 mW/cm^2, and an increased range of wavelength promoted an excellent improvement of the light-driven hydrogen production, achieving TONs of 70 and 37 for the FeFeOH and NCOFeFe, respectively. Molecular aggregation phenomena due to the hydrophobic nature of the NCOFeFe precursor was suggested to explain the decrease of available active diiron centers and, as a consequence, the decrease in photocatalytic activity compared to that shown by FeFeOH.

The immobilization of NCOFeFe on ethylene-bridged PMO allowed working in a completely aqueous medium but led to lower hydrogen evolution yields, likely due to some blocking of the active sites. The EthanePMO@NCOFeFe heterogeneous catalyst

reached a TON of 5, indicating a lower activity than the homogeneous complexes but comparable to other immobilized [FeFe]-hydrogenase biomimetic models, which were previously reported.

Supplementary Materials: The following are available online at https://www.mdpi.com/article/10.3390/catal12030254/s1, Figure S1: FTIR-ATR monitoring of the reaction between the FeFeOH catalyst and 3-isocyanopropyltriethoxysilane, Figure S2: ^{1}H-NMR spectra of the FeFeOH diiron complex, Figure S3: ^{13}C-NMR and ^{13}C DEPT-NMR spectra of the FeFeOH diiron complex, Figure S4: ^{1}H-NMR spectra of the NCOFeFe monosilane precursor, Figure S5: ^{13}C-NMR and ^{13}C DEPT-NMR spectra of the NCOFeFe diiron complex, Figure S6: Control photocatalytic experiments without the FeFeOH catalyst (a) and photosensitizer (b), Figure S7: UV–VIS spectra of FeFeOH (A) and NCOFeFe (B) under analogous standard conditions (0.84 mM of the homogeneous catalyst, 1 M of the acetate buffer at pH 5.0, and ACN/H_2O with a 11.8 vol% organic phase) at t = 0 h and t = 4 h, Figure S8: FTIR-ATR spectra of 0.71 mM FeFeOH (A) and 0.71 mM NCOFeFe (B) in ACN at t = 0 h and t = 4 h, Figure S9: Photocatalytic hydrogen production under standard conditions (2 mg of EthanePMO@NCOFeFe, 0.5 mM of $Ru(bpy)_3^{2+}$, 100 mM of ascorbic acid, and 1 M of the acetate buffer at pH 5.0) in the heterogeneous phase (milli-Q water solution) after 26 h, Table S1: Photocatalytic performance of diiron molecular catalysts in light-driven hydrogen production. References [18,19,22,24,25,27] are cited in the Supplementary Materials.

Author Contributions: Conceptualization, D.E., C.J.-S., H.T., S.O. and F.J.R.-S.; investigation, J.A.-G. and M.V.P.; writing—original draft preparation, J.A.-G.; writing—review and editing, J.A.-G., D.E., M.V.P., S.O. and F.J.R.-S.; supervision, C.J.-S. and H.T. All authors have read and agreed to the published version of the manuscript.

Funding: This research was funded by Ramon Areces Foundation (RAMON ARECES 16), Spanish Ministry of Science, Innovation and Universities (MICIU, FPU teaching and research fellowship (FPU17/03981), Project RTI2018-101611-B-I00), Olle Engkvist Foundation (200-0523), and Swedish Research Council (2015-04640).

Acknowledgments: J.A.-G., D.E., C.J.-S. and F.J.R.-S. wish to acknowledge the financial support from Spanish Ministry of Science, Innovation and Universities for an FPU teaching and research fellowship (FPU17/03981) and Project RTI2018-101611-B-I00,Andalusian Regional Government (FQM-346 group), and Feder Funds. M.V.P., H.T. and S.O. wish to acknowledge the financial support from Olle Engkvist Foundation (200-0523), and Swedish Research Council (2015-04640).

Conflicts of Interest: The authors declare no conflict of interest.

References

1. Dresselhaus, M.S.; Thomas, I.L. Alternative energy technologies. *Nature* **2001**, *414*, 332–337. [CrossRef] [PubMed]
2. Panwar, N.L.; Kaushik, S.C.; Kothari, S. Role of renewable energy sources in environmental protection: A review. *Renew. Sustain. Energy Rev.* **2011**, *15*, 1513–1524. [CrossRef]
3. Gielen, D.; Boshell, F.; Saygin, D.; Bazilian, M.D.; Wagner, N.; Gorini, R. The role of renewable energy in the global energy transformation. *Energy Strateg. Rev.* **2019**, *24*, 38–50. [CrossRef]
4. Ismail, A.A.; Bahnemann, D.W. Photochemical splitting of water for hydrogen production by photocatalysis: A review. *Sol. Energy Mater. Sol. Cells* **2014**, *128*, 85–101. [CrossRef]
5. Acar, C.; Dincer, I.; Naterer, G.F. Review of photocatalytic water-splitting methods for sustainable hydrogen production. *Int. J. Energy Res.* **2016**, *40*, 1449–1473. [CrossRef]
6. Chen, S.; Takata, T.; Domen, K. Particulate photocatalysts for overall water splitting. *Nat. Rev. Mater.* **2017**, *2*, 17050. [CrossRef]
7. Kabir, E.; Kumar, P.; Kumar, S.; Adelodun, A.A.; Kim, K.-H. Solar energy: Potential and future prospects. *Renew. Sustain. Energy Rev.* **2018**, *82*, 894–900. [CrossRef]
8. Corredor, J.; Rivero, M.J.; Rangel, C.M.; Gloaguen, F.; Ortiz, I. Comprehensive review and future perspectives on the photocatalytic hydrogen production. *J. Chem. Technol. Biotechnol.* **2019**, *94*, 3049–3063. [CrossRef]
9. Hosseini, S.E.; Wahid, M.A. Hydrogen production from renewable and sustainable energy resources: Promising green energy carrier for clean development. *Renew. Sustain. Energy Rev.* **2016**, *57*, 850–866. [CrossRef]
10. Abe, J.O.; Popoola, A.P.I.; Ajenifuja, E.; Popoola, O.M. Hydrogen energy, economy and storage: Review and recommendation. *Int. J. Hydrogen Energy* **2019**, *44*, 15072–15086. [CrossRef]
11. Frey, M. Hydrogenases: Hydrogen-Activating Enzymes. *ChemBioChem* **2002**, *3*, 153–160. [CrossRef]
12. Vignais, P.M.; Billoud, B. Occurrence, Classification, and Biological Function of Hydrogenases: An Overview. *Chem. Rev.* **2007**, *107*, 4206–4272. [CrossRef]

13. Lubitz, W.; Ogata, H.; Rüdiger, O.; Reijerse, E. Hydrogenases. *Chem. Rev.* **2014**, *114*, 4081–4148. [CrossRef] [PubMed]
14. Sun, L.; Akermark, B.; Ott, S. Iron hydrogenase active site mimics in supramolecular systems aiming for light-driven hydrogen production. *Coord. Chem. Rev.* **2005**, *249*, 1653–1663. [CrossRef]
15. Simmons, T.R.; Berggren, G.; Bacchi, M.; Fontecave, M.; Artero, V. Mimicking hydrogenases: From biomimetics to artificial enzymes. *Coord. Chem. Rev.* **2014**, *270–271*, 127–150. [CrossRef]
16. Lomoth, R.; Ott, S. Introducing a dark reaction to photochemistry: Photocatalytic hydrogen from [FeFe] hydrogenase active site model complexes. *Dalton Trans.* **2009**, 9952–9959. [CrossRef]
17. Junge, H.; Rockstroh, N.; Fischer, S.; Brückner, A.; Ludwig, R.; Lochbrunner, S.; Kühn, O.; Beller, M. Light to Hydrogen: Photocatalytic Hydrogen Generation from Water with Molecularly-Defined Iron Complexes. *Inorganics* **2017**, *5*, 14. [CrossRef]
18. Na, Y.; Wang, M.; Pan, J.; Zhang, P.; Åkermark, B.; Sun, L. Visible Light-Driven Electron Transfer and Hydrogen Generation Catalyzed by Bioinspired [2Fe2S] Complexes. *Inorg. Chem.* **2008**, *47*, 2805–2810. [CrossRef]
19. Streich, D.; Astuti, Y.; Orlandi, M.; Schwartz, L.; Lomoth, R.; Hammarström, L.; Ott, S. High-Turnover Photochemical Hydrogen Production Catalyzed by a Model Complex of the [FeFe]-Hydrogenase Active Site. *Chem. Eur. J.* **2010**, *16*, 60–63. [CrossRef]
20. Zhang, P.; Wang, M.; Na, Y.; Li, X.; Jiang, Y.; Sun, L. Homogeneous photocatalytic production of hydrogen from water by a bioinspired [Fe_2S_2] catalyst with high turnover numbers. *Dalton Trans.* **2010**, *39*, 1204–1206. [CrossRef]
21. Wang, F.; Wang, W.-G.; Wang, X.-J.; Wang, H.-Y.; Tung, C.-H.; Wu, L.-Z. A Highly Efficient Photocatalytic System for Hydrogen Production by a Robust Hydrogenase Mimic in an Aqueous Solution. *Angew. Chem. Int. Ed.* **2011**, *50*, 3193–3197. [CrossRef] [PubMed]
22. Cao, W.-N.; Wang, F.; Wang, H.-Y.; Chen, B.; Feng, K.; Tung, C.-H.; Wu, L.-Z. Photocatalytic hydrogen production from a simple water-soluble [FeFe]-hydrogenase model system. *Chem. Commun.* **2012**, *48*, 8081. [CrossRef] [PubMed]
23. Li, X.; Wang, M.; Chen, L.; Wang, X.; Dong, J.; Sun, L. Photocatalytic Water Reduction and Study of the Formation of FeIFe0 Species in Diiron Catalyst Sytems. *ChemSusChem* **2012**, *5*, 913–919. [CrossRef] [PubMed]
24. Pullen, S.; Fei, H.; Orthaber, A.; Cohen, S.M.; Ott, S. Enhanced Photochemical Hydrogen Production by a Molecular Diiron Catalyst Incorporated into a Metal–Organic Framework. *J. Am. Chem. Soc.* **2013**, *135*, 16997–17003. [CrossRef] [PubMed]
25. Jian, J.-X.; Ye, C.; Wang, X.-Z.; Wen, M.; Li, Z.-J.; Li, X.-B.; Chen, B.; Tung, C.-H.; Wu, L.-Z. Comparison of H_2 photogeneration by [FeFe]-hydrogenase mimics with CdSe QDs and $Ru(bpy)_3Cl_2$ in aqueous solution. *Energy Environ. Sci.* **2016**, *9*, 2083–2089. [CrossRef]
26. Wang, X.-B.; Zheng, H.-Q.; Rao, H.; Yao, H.-C.; Fan, Y.-T.; Hou, H.-W. Synthesis of a new iron-sulfur cluster compound and its photocatalytic H_2 evolution activity through visible light irradiation. *Appl. Organomet. Chem.* **2016**, *30*, 638–644. [CrossRef]
27. Himiyama, T.; Waki, M.; Esquivel, D.; Onoda, A.; Hayashi, T.; Van Der Voort, P.; Inagaki, S. A Heterogeneous Hydrogen-Evolution Catalyst Based on a Mesoporous Organosilica with a Diiron Catalytic Center Modelling [FeFe]-Hydrogenase. *ChemCatChem* **2018**, *10*, 4894–4899. [CrossRef]
28. Rakowski DuBois, M.; DuBois, D.L. The roles of the first and second coordination spheres in the design of molecular catalysts for H_2 production and oxidation. *Chem. Soc. Rev.* **2009**, *38*, 62–72. [CrossRef]
29. Felton, G.A.N.; Mebi, C.A.; Petro, B.J.; Vannucci, A.K.; Evans, D.H.; Glass, R.S.; Lichtenberger, D.L. Review of electrochemical studies of complexes containing the Fe_2S_2 core characteristic of [FeFe]-hydrogenases including catalysis by these complexes of the reduction of acids to form dihydrogen. *J. Organomet. Chem.* **2009**, *694*, 2681–2699. [CrossRef]
30. Wang, M.; Chen, L.; Li, X.; Sun, L. Approaches to efficient molecular catalyst systems for photochemical H_2 production using [FeFe]-hydrogenase active site mimics. *Dalton Trans.* **2011**, *40*, 12793. [CrossRef]
31. Rauchfuss, T.B. Diiron Azadithiolates as Models for the [FeFe]-Hydrogenase Active Site and Paradigm for the Role of the Second Coordination Sphere. *Acc. Chem. Res.* **2015**, *48*, 2107–2116. [CrossRef] [PubMed]
32. Darmon, J.M.; Kumar, N.; Hulley, E.B.; Weiss, C.J.; Raugei, S.; Bullock, R.M.; Helm, M.L. Increasing the rate of hydrogen oxidation without increasing the overpotential: A bio-inspired iron molecular electrocatalyst with an outer coordination sphere proton relay. *Chem. Sci.* **2015**, *6*, 2737–2745. [CrossRef] [PubMed]
33. Wen, M.; Li, X.-B.; Jian, J.-X.; Wang, X.-Z.; Wu, H.-L.; Chen, B.; Tung, C.-H.; Wu, L.-Z. Secondary coordination sphere accelerates hole transfer for enhanced hydrogen photogeneration from [FeFe]-hydrogenase mimic and CdSe QDs in water. *Sci. Rep.* **2016**, *6*, 29851. [CrossRef] [PubMed]
34. Brezinski, W.P.; Karayilan, M.; Clary, K.E.; McCleary-Petersen, K.C.; Fu, L.; Matyjaszewski, K.; Evans, D.H.; Lichtenberger, D.L.; Glass, R.S.; Pyun, J. Macromolecular Engineering of the Outer Coordination Sphere of [2Fe-2S] Metallopolymers to Enhance Catalytic Activity for H_2 Production. *ACS Macro Lett.* **2018**, *7*, 1383–1387. [CrossRef]
35. Amaro-Gahete, J.; Pavliuk, M.V.; Tian, H.; Esquivel, D.; Romero-Salguero, F.J.; Ott, S. Catalytic systems mimicking the [FeFe]-hydrogenase active site for visible-light-driven hydrogen production. *Coord. Chem. Rev.* **2021**, *448*, 214172. [CrossRef]
36. Jiang, X.; Wang, H.; Feng, Y.; Gu, E.; Liu, X. Electrochemically probing the correlation between photo-induced CO-releasing behaviours and their LUMO energies of three diiron carbonyl complexes. *Inorganica Chim. Acta* **2017**, *464*, 125–131. [CrossRef]
37. Katz, S.; Noth, J.; Horch, M.; Shafaat, H.S.; Happe, T.; Hildebrandt, P.; Zebger, I. Vibrational spectroscopy reveals the initial steps of biological hydrogen evolution. *Chem. Sci.* **2016**, *7*, 6746–6752. [CrossRef]
38. Attaei, M.; Loureiro, M.; do Vale, M.; Condeço, J.; Pinho, I.; Bordado, J.; Marques, A. Isophorone Diisocyanate (IPDI) Microencapsulation for Mono-Component Adhesives: Effect of the Active H and NCO Sources. *Polymers* **2018**, *10*, 825. [CrossRef]

39. Cui, H.; Hu, M.; Wen, H.; Chai, G.; Ma, C.; Chen, H.; Chen, C. Efficient [FeFe] hydrogenase mimic dyads covalently linking to iridium photosensitizer for photocatalytic hydrogen evolution. *Dalton Trans.* **2012**, *41*, 13899. [CrossRef]
40. Caplins, B.W.; Lomont, J.P.; Nguyen, S.C.; Harris, C.B. Vibrational cooling dynamics of a [FeFe]-hydrogenase mimic probed by time-resolved infrared spectroscopy. *J. Phys. Chem. A* **2014**, *118*, 11529–11540. [CrossRef]
41. Haley, A.L.; Broadbent, L.N.; McDaniel, L.S.; Heckman, S.T.; Hinkle, C.H.; Gerasimchuk, N.N.; Hershberger, J.C.; Mebi, C.A. [Fe–Fe] hydrogenase models: Iron(I)-carbonyl clusters coupled to alpha- and para-toluenethiolate ligands. *Polyhedron* **2016**, *114*, 218–224. [CrossRef]
42. Zhang, X.; Zhang, T.; Li, B.; Zhang, G.; Hai, L.; Ma, X.; Wu, W. Direct synthesis of phenol by novel [FeFe]-hydrogenase model complexes as catalysts of benzene hydroxylation with H_2O_2. *RSC Adv.* **2017**, *7*, 2934–2942. [CrossRef]
43. Zhang, X.; Liu, L.; Li, Y. Synthesis and Benzene Hydroxylation Properties of Amino Substituted [FeFe]-Hydrogenase Model Compounds. *Catal. Lett.* **2020**, *150*, 2879–2885. [CrossRef]
44. Van Der Voort, P.; Esquivel, D.; De Canck, E.; Goethals, F.; Van Driessche, I.; Romero-Salguero, F.J. Periodic Mesoporous Organosilicas: From simple to complex bridges; a comprehensive overview of functions, morphologies and applications. *Chem. Soc. Rev.* **2013**, *42*, 3913–3955. [CrossRef] [PubMed]
45. Esquivel, D.; Amaro-Gahete, J.; Caballero-Casero, N.; Jiménez-Sanchidrián, C.; Ruiz, J.R.; Rubio, S.; Van Der Voort, P.; Romero-Salguero, F.J. Tailoring Bifunctional Periodic Mesoporous Organosilicas for Cooperative Catalysis. *ACS Appl. Nano Mater.* **2020**, *3*, 2373–2382. [CrossRef]
46. López, M.I.; Esquivel, D.; Jiménez-Sanchidrián, C.; Romero-Salguero, F.J.; Van Der Voort, P. A "one-step" sulfonic acid PMO as a recyclable acid catalyst. *J. Catal.* **2015**, *326*, 139–148. [CrossRef]
47. Kaczmarek, A.M.; Abednatanzi, S.; Esquivel, D.; Krishnaraj, C.; Jena, H.S.; Wang, G.; Leus, K.; Van Deun, R.; Romero–Salguero, F.J.; Van Der Voort, P. Amine-containing (nano-) Periodic Mesoporous Organosilica and its application in catalysis, sorption and luminescence. *Microporous Mesoporous Mater.* **2020**, *291*, 109687. [CrossRef]
48. Cornelius, M.; Hoffmann, F.; Fröba, M. Periodic Mesoporous Organosilicas with a Bifunctional Conjugated Organic Unit and Crystal-like Pore Walls. *Chem. Mater.* **2005**, *17*, 6674–6678. [CrossRef]
49. López, M.I.; Esquivel, D.; Jiménez-Sanchidrián, C.; Van Der Voort, P.; Romero-Salguero, F.J. Thiol-Functionalized Ethylene Periodic Mesoporous Organosilica as an Efficient Scavenger for Palladium: Confirming the Homogeneous Character of the Suzuki Reaction. *Materials* **2020**, *13*, 623. [CrossRef]
50. Kaczmarek, A.M.; Van Der Voort, P. Light-Emitting Lanthanide Periodic Mesoporous Organosilica (PMO) Hybrid Materials. *Materials* **2020**, *13*, 566. [CrossRef]
51. Takahashi, F.; Jin, J. Self-quenching in the electrochemiluminescence of $Ru(bpy)_3^{2+}$ using ascorbic acid as co-reactant. *Luminescence* **2008**, *23*, 121–125. [CrossRef] [PubMed]
52. Shan, B.; Baine, T.; Ma, X.A.N.; Zhao, X.; Schmehl, R.H. Mechanistic Details for Cobalt Catalyzed Photochemical Hydrogen Production in Aqueous Solution: Efficiencies of the Photochemical and Non-Photochemical Steps. *Inorg. Chem.* **2013**, *52*, 4853–4859. [CrossRef]
53. Zhu, D.; Xiao, Z.; Liu, X. Introducing polyethyleneimine (PEI) into the electrospun fibrous membranes containing diiron mimics of [FeFe]-hydrogenase: Membrane electrodes and their electrocatalysis on proton reduction in aqueous media. *Int. J. Hydrogen Energy* **2015**, *40*, 5081–5091. [CrossRef]
54. Wang, W.; Yu, T.; Zeng, Y.; Chen, J.; Yang, G.; Li, Y. Enhanced photocatalytic hydrogen production from an MCM-41-immobilized photosensitizer–[Fe–Fe] hydrogenase mimic dyad. *Photochem. Photobiol. Sci.* **2014**, *13*, 1590–1597. [CrossRef] [PubMed]
55. Shylin, S.I.; Pavliuk, M.V.; D'Amario, L.; Mamedov, F.; Sá, J.; Berggren, G.; Fritsky, I.O. Efficient visible light-driven water oxidation catalysed by an iron(IV) clathrochelate complex. *Chem. Commun.* **2019**, *55*, 3335–3338. [CrossRef] [PubMed]
56. Kayanuma, M.; Stoll, T.; Daniel, C.; Odobel, F.; Fortage, J.; Deronzier, A.; Collomb, M.-N. A computational mechanistic investigation of hydrogen production in water using the $[Rh\ III\ (dmbpy)_2Cl_2]^+$/$[Ru\ II\ (bpy)_3]^{2+}$/ascorbic acid photocatalytic system. *Phys. Chem. Chem. Phys.* **2015**, *17*, 10497–10509. [CrossRef] [PubMed]
57. Yang, Q.; Liu, J.; Yang, J.; Zhang, L.; Feng, Z.; Zhang, J.; Li, C. Acid catalyzed synthesis of ordered bifunctionalized mesoporous organosilicas with large pore. *Microporous Mesoporous Mater.* **2005**, *77*, 257–264. [CrossRef]
58. Yang, Q.; Liu, J.; Yang, J.; Kapoor, M.P.; Inagaki, S.; Li, C. Synthesis, characterization, and catalytic activity of sulfonic acid-functionalized periodic mesoporous organosilicas. *J. Catal.* **2004**, *228*, 265–272. [CrossRef]